

VIP Very Important Paper



# Formation of the Solid Electrolyte Interphase at Constant Potentials: A Model Study on Highly Oriented Pyrolytic Graphite

Byron K. Antonopoulos,<sup>[a]</sup> Filippo Maglia,<sup>[a]</sup> Felix Schmidt-Stein,<sup>[a]</sup> Jan P. Schmidt,<sup>[a]</sup> and Harry E. Hoster\*,<sup>[b]</sup>

The solid electrolyte interphase (SEI) on graphite anodes is a key enabler for rechargeable lithium-ion batteries (LIBs). It ensures that only  $\text{Li}^+$  ions and no damaging electrolyte components enter the anode and hinders electrolyte decomposition. Its growth should be confined to the initial SEI formation process and stop once the battery is in operation to avoid capacity/power loss. In technical LIB cells, the SEI is formed at constant current, with the potential of the graphite anode slowly drifting from higher to lower voltages. SEI formation rate, composition, and structure depend on the potential and on the chemical properties of the anode surface. Here, we characterize SEIs formed at constant potentials on the chemically inactive basal

plane of highly oriented pyrolytic graphite (HOPG). X-ray photoemission spectroscopy (XPS) detects carbonate species only at lower formation potentials. Cyclic voltammetry (CV) and Electrochemical Impedance Spectroscopy (EIS) with  $\text{Fc}/\text{Fc}^+$  as an electrochemical probe demonstrate how the formation potential influences ion transport and electrochemical kinetics to and at the anode surface, respectively. Breaking the EIS data down to a Distribution of Relaxation Times (DRT) reveals distinct kinetics and transport related peaks with varying Arrhenius-type temperature dependencies. We discuss our findings in the context of previous electrochemical studies and existing SEI models and of SEI formation protocols suitable for industry.

## 1. Introduction

Li-ion batteries (LIB) have become a technologic and commercial success through the combination of graphitic carbon and a transition metal oxide as negative and positive electrode, respectively. Li intercalated in graphite is thermodynamically slightly more stable than in metallic form: Li-ions reversibly (de)intercalate into/out of graphite at  $\sim 100 \text{ mV}$  vs.  $\text{Li}/\text{Li}^+$ . This helps to avoid Li dendrites. An ideal LIB electrolyte would combine high ionic conductivity, diffusivity, broad temperature stability, and stability against electrochemical decomposition at anode or cathode. Commercially available electrolytes have been engineered to come close to those ideals, but do not quite reach all of them simultaneously.<sup>[1–5]</sup> In particular, electro-

chemical decomposition at the negative electrode is thermodynamically possible; hence only kinetic hindrances of those side reactions make the thousands of charge/discharge cycles possible that can be achieved, e.g., with electrolytes consisting of alkyl carbonates as solvents and  $\text{LiPF}_6$  as conducting salt.<sup>[6,7]</sup> Kinetic suppression of ongoing electrolyte decomposition is achieved through the initial “formation” step applied to all commercial LIBs. In that first negative polarization of the graphite anode, the electrolyte is decomposed in a controlled way into a passivation layer that, once sufficient thickness is reached, will kinetically suppress ongoing electrolyte decomposition.<sup>[8,9]</sup> Another key property gave this passivation layer the name “solid electrolyte interphase” (SEI): It acts as solid electrolyte for  $\text{Li}^+$  transport between the liquid electrolyte and the graphite electrode. Furthermore, it acts as a filter, preventing co-intercalation of other electrolyte components (e.g. solvent), which would otherwise quickly destroy the graphite electrode structure. In real systems, further electrolyte decomposition is not completely suppressed and continues, yet at a small rate, which grows the SEI over time. The two most prominent negative effects of this ongoing process are (i) increasingly sluggish  $\text{Li}^+$  transport kinetics through the SEI and (ii) irreversible incorporation of  $\text{Li}^+$  into the SEI, thus lowering the cell capacity. Formation and further development of the SEI depend on electrolyte and electrode composition and preparation, formation parameters and contaminations including those produced during the cell life.<sup>[8,10–21]</sup>

From an interfacial electrochemistry perspective, the SEI can be handled as a nearly homogeneous adlayer with conducting channels. Perpendicular to the electrode, one can imagine a sequence electrode | SEI(compact layer) | SEI(porous part) | elec-

[a] B. K. Antonopoulos, Dr. F. Maglia, Dr. F. Schmidt-Stein, Dr. J. P. Schmidt  
BMW Group  
Petuelring 130, 80788 München, Germany

[b] Prof. Dr. H. E. Hoster  
Dep. of Chemistry  
Lancaster University  
Lancaster, LA1 4YB, UK  
and

ALISTORE European Research Institute CNRS FR 3104  
Hub de l'Energie  
Rue Baudelocque, 80039 Amiens, France  
and  
The Faraday Institution  
Quad One, Harwell Science and Innovation Campus  
Didcot, UK  
+44 7842 831633  
E-mail: h.hoster@lancaster.ac.uk

 Supporting Information and the ORCID identification number(s) for the author(s) of this article can be found under:  
<https://doi.org/10.1002/batt.201800029>

trolyte.<sup>[22]</sup> The compact layer was found to partially consist of inorganic (Li-containing) species, which were hypothesized to be formed only once lower potentials are reached during the formation process, then consuming Li<sup>+</sup> and parts of the organic SEI components formed at higher potentials ("two-step mechanism"<sup>[19,23,24]</sup>). It is now well accepted that the safe and reliable operation of rechargeable LIBs demands understanding and control of side reactions, many of which are influenced by the electrode potential and the local surface chemistry and structure. Hence, in analogy to fundamental research in the electrocatalysis community,<sup>[25,26]</sup> deeper insights require studies at well-defined model surfaces under potentiostatic conditions, and involving both electrochemical techniques as well as high resolution surface microscopy and spectroscopy.<sup>[20,21,27–35]</sup> Particularly the SEI on Glassy Carbon (GC) was studied extensively by Tang et al.<sup>[23,36,37]</sup> and others.<sup>[38,39]</sup> For commercial electrolyte, Fc/Fc<sup>+</sup> as an electrochemical probe for the effect of the SEI on ion transport and electrochemical kinetics revealed that SEI formation can be broken down to two key steps at ~700 and ~400 mV vs. Li/Li<sup>+</sup>.<sup>[35]</sup> More recently, we and others studied the formation of LiF, a frequently observed SEI component, on smooth carbon and metal single crystal surfaces and demonstrated the importance of surface electrocatalysis.<sup>[40–42]</sup>

For the present study, we have chosen the basal plane of highly oriented pyrolytic graphite (HOPG) as a model electrode, and using a cell setup that resembles the pressure conditions of LIB electrodes. Since this surface exposes few chemically reactive sites (i.e., step edges and defects), it is electrocatalytically virtually inert. Hence, surface reactions will be dominated by the availability of reactants and the electrochemical potential. In analogy to studies on glassy carbon,<sup>[38,39]</sup> the low surface area of HOPG<sup>[35]</sup> allows applying potential steps followed by constant-potential periods, which on technical high-surface area electrodes would cause high current peaks, long relaxation times, and inhomogeneous potential distribution. In the electrochemical part of our experiments, we followed the protocols that Tang et al. used in their model studies at glassy carbon: SEI formation at four different potentials and probing the resulting SEI properties using cyclic voltammetry (CV) and electrochemical impedance spectroscopy (EIS) of dissolved Fc/Fc<sup>+</sup>. Beyond that, we analyzed the potential-dependent composition of the SEI by ex-situ X-ray photoelectron spectroscopy (XPS), and we broke down the EIS data into a Distribution of Relaxation Times (DRT). We discuss the findings of our multi-method study in the context of previous electrochemical model studies and existing SEI models<sup>[22,23,35–39]</sup> and suggest how our findings may inform more efficient SEI formation protocols in industry.

## Experimental

Basal plane HOPG (mosaic spread 0.8° ± 0.2°, Plano GmbH, Germany) was cleaned with adhesive tape before being used as a model electrode surface. It was fully covered by PET tape (T 851, 3 M, USA) leaving exposed a well-defined basal circular area with 4 mm diameter to the electrolyte. The sample was finally mounted on the sample holder and then dried at 60 °C for 12 h at a pressure

~10<sup>-2</sup> mbar in a vacuum oven (Glass Oven B-585 Drying, BÜCHI Labortechnik AG, Switzerland) before being transferred without atmosphere contact into an Argon filled glove box. The other cell components were cleaned with 2-propanol and demineralized water in an ultrasonic bath and then dried at 60 °C before being transferred into the glove box for cell assembly. The glove box contained < 0.1 ppm water and < 3 ppm oxygen.

All experiments were performed several times in order to ensure reproducibility. Conspicuously deviating results were not considered. This was particularly important as some of the manually affected experimental side parameters (e.g. injection speed and position, sample preparation and washing, position of single cell features etc.) can vary. Accuracy of quantitative values (number of digits) given in this work is based on typical variances.

## Electrochemistry

We used a closed 3-electrode T-cell with the option to connect a further feature (designed and manufactured by rhd instruments GmbH & Co. KG, Germany; see also their recently released "TSC battery standard"). Li foil (ca. 500 µm, Alfa Aesar, UK) served as counter and reference electrode. The sample was separated by a Whatman GF/A glass fiber separator (Sigma Aldrich, Germany) soaked in 75 µl BASF LP572 (EC:EMC 3:7, 1 M LiPF<sub>6</sub>, 2% wt VC, BASF, Germany). The CE and sample were pressed against each other by a spring. The sample holder included a Pt100 temperature sensor for sample temperature control. The second vertical connector ("syringe connector") was used to connect a Hamilton Gastight syringe (VWR, Germany) via a glass capillary. The syringe contained around 30 µl electrolyte enriched with 10 mMol ferrocene and ferrocenium hexafluorophosphate (Fc and Fc<sup>+</sup>, respectively, both from Sigma Aldrich, Germany), of which 25 µl were injected into the cell, yielding a Fc/Fc<sup>+</sup> concentration of 2.5 mMol L<sup>-1</sup>. For SEI-free experiments, no syringe was connected and the syringe connector was sealed with an appropriate plug. 100 µl of electrolyte with 2.5 mMol Fc/Fc<sup>+</sup> concentration was used.

The assembled cell was mounted on a Microcell HC cell holder connected to a Eurotherm temperature controller (both rhd instruments GmbH & Co. KG, Germany). Unless otherwise mentioned, all electrochemical experiments were performed at 20 °C. The electrochemical instrumentation was an Autolab M101 Potentiostat with FRA32M impedance spectroscopy module controlled by the manufacturer software Nova (Deutsche METROHM GmbH & Co. KG, Germany). CV experiments consisted of 5 cycles, but only the fifth was processed. EIS experiments were obtained around OCP with an amplitude of 10 mV using 50 logarithmically distributed frequencies in the range 500 kHz–0.1 Hz.

HOPG basal plane is a surface with large flat terraces, though the above described preparation method cannot avoid inducing edge defect sites facilitating Li<sup>+</sup> intercalation. To make sure that possibly intercalated residuals from previous experiments were stripped off by the adhesive tape, we checked the open circuit potential (OCP) after cell assembly. The cell was discarded if OCP was below 3 V vs. Li/Li<sup>+</sup>. All electrochemical potentials in this paper describe the potential of the working electrode in the three-electrode setup and refer to the Li metal reference electrode, thus are given vs. Li/Li<sup>+</sup>. Due to the high electronic conductivity of HOPG through-plane potential gradients lie in the sub-µV region and are therefore neglected.

## X-Ray Photoelectron Spectroscopy

The sample holder covered by double-sided XPS compatible adhesive tape was dried similar to the HOPG. After electrochemical

treatment the cells were disassembled in the glove box for further spectroscopic analysis of the electrodes. Samples were rinsed with 1 ml dimethyl carbonate (DMC, Sigma Aldrich, Germany) using a pipette and then fixed on the sample holder. To transfer the sample from the glove box to the spectrometer it was introduced into a transfer vessel (Model 04-110A, Physical Electronics GmbH, Germany) and sealed, which itself was further vacuum sealed into an aluminum based pouch bag. The sample could be verifiably transferred into the analysis chamber without any atmosphere contact. Spectra were recorded with a PHI 5000 spectrometer (Physical Electronics GmbH, Germany) using Al K $\alpha$  radiation ( $h\nu = 1486.6$  eV) under ultrahigh vacuum conditions. Sputtering was performed using an Ar $^+$  gun with 0.5 kV and a 4×4 mm $^2$  spot size, using a current that correlates to 0.25 nm min $^{-1}$  as calibrated on Si/SiO $_2$ . Spectra were shifted based on the C 1s graphite binding energy at 284.8 eV on pristine HOPG. Atomic concentrations were determined via the analysis software Phi MultiPak.

## 2. Results and Discussion

### 2.1. Potentiostatic SEI Formation

To allow direct comparison with the results previously reported for GC electrodes,<sup>[23]</sup> we formed SEIs at 600, 450, 300 and 100 mV. Lower formation potentials were not considered, as no distinct reactions take place at potentials <100 mV, whilst potentials >600 mV do not form a passivating SEI on HOPG.<sup>[28,29,35]</sup> In order to achieve a comparable set of SEIs we defined three equipotent cutoff parameters terminating the potentiostatic polarization step, namely the current density, charge density and formation time at 4  $\mu\text{A cm}^{-2}$ , 10 mC cm $^{-2}$  and 600 s, respectively.

An exemplary reduction current density transient  $j$  after applying 100 mV is presented in Figure 1a. The profiles looked very similar for the other formation potentials. For better visibility, Figure 1b and c display two characteristic current density regimes. After the potential is applied we obtained a high reductive current, which drops to less than 5% within the first 500 ms. The drop includes a shoulder at 50 ms (indicated by the arrow), though passivates after around 100 s. No systematic relation could be found between the final passivation current  $j_{\text{Pass}}$  indicated in Figure 1c and the applied potential, though the value was always below 10  $\mu\text{A cm}^{-2}$ . Figure 1b includes an exponential fit (dashed line) with time constant 133 ms (corresponds to 7.5 s $^{-1}$ ).

In contrast to composite carbon electrodes, which suffer from electrolyte decomposition even in later cycles due to particle breathing,<sup>[22]</sup> the non-intercalating HOPG electrode should be irreversibly passivated during this first polarization. Apart from electrochemical electrolyte reduction, the current response to the potentiostatic step may result from three further contributions: (i) charging of the double layer capacitance, (ii) Li $^+$  intercalation into the HOPG at step edges and (iii) other irreversible side reactions (e.g. production of dissolved species). Although the setup is optimized in order to avoid those current overlaps, we experimentally tested for their possible presence and significance. As shown in more details in the Supplementary Information (SI), their contributions are

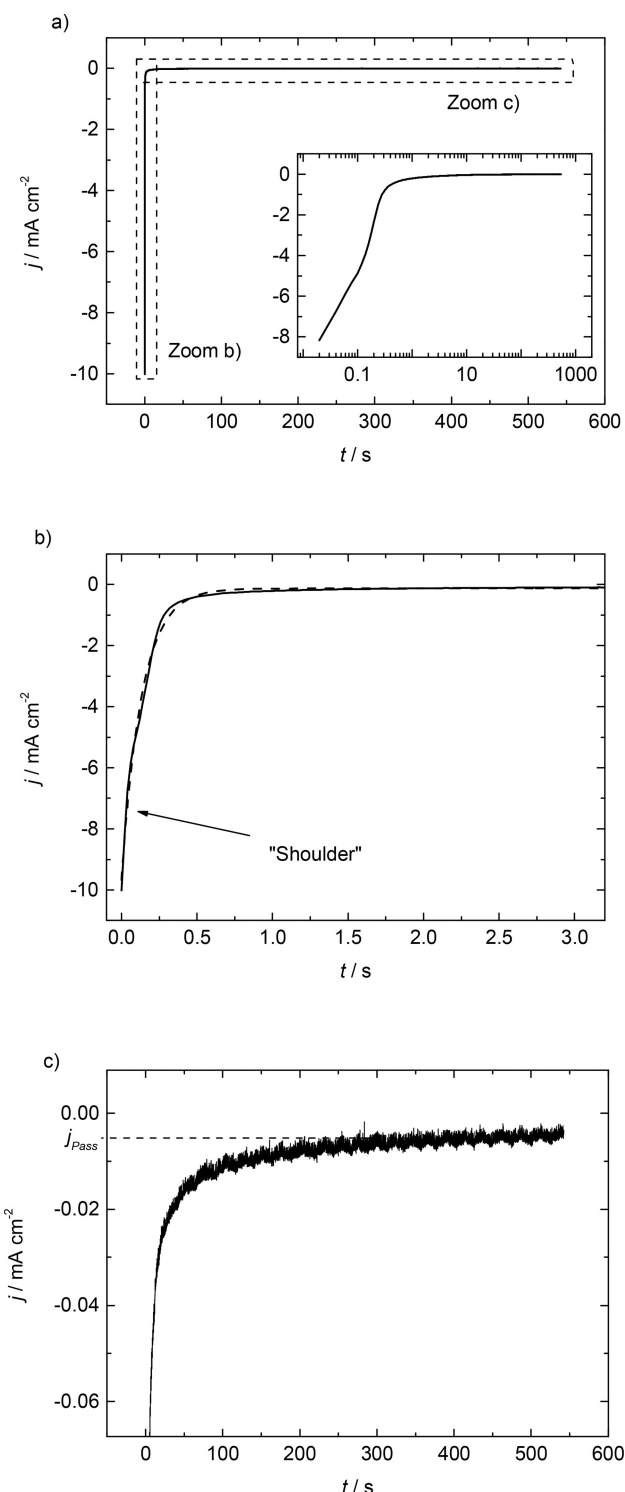


**Figure 1.** Current density  $j$  during a potentiostatic formation procedure on HOPG at 100 mV in neat electrolyte, inset with logarithmic abscissa. b) and c) are detailed zooms of a). The dashed line in b) indicates the exponential fit with an exponential coefficient 7.5 s $^{-1}$ .

negligible. For instance, the characteristic time constants of double layer charging currents calculated in the SI would be in the order of magnitude of 10 $^{-6}$  s, which is significantly smaller than the 133 ms resulting from the fit in Figure 1b. Hence, the 100s-scale relaxation in Figure 1c must reflect the increase of a

(quasi-)resistance, namely the expected and desired self-passivating nature of the electrochemical SEI formation.

## 2.2. XPS

Ex-situ X-ray photoelectron spectroscopy (XPS) was used to analyze the chemical compositions of SEIs formed at 600, 450, 300 and 100 mV. Figure 2 shows spectra of the C1s, O1s and F1s regions. Li1s spectra of all SEIs and F1s spectrum of 600 mV SEI were recorded but did not show any features beyond noise and are therefore not shown. All plotted spectra belong to samples “as transferred”, without any layers removed by Ar<sup>+</sup> sputtering. Even three minutes of sputtering made the O1s signal disappear completely, which is not surprising given that SEIs on basal planes are known to be significantly thinner than on edge planes.<sup>[21,27]</sup> The peak positions in Figure 2 are in good agreement with features in previous XPS analyses of SEI layers.<sup>[43–57]</sup>

Looking at the C1s region, both lower potential (300 and 100 mV) SEIs show a stronger response in the C=O region as compared to the high-potential SEIs (600 and 450 mV). Li<sub>2</sub>CO<sub>3</sub> related features are only distinctive for the 100 mV SEI. The 600 mV SEI appears to have a higher amount of C–O bonds. Alkyl carbonates, which are typical solvent decomposition products,<sup>[22,58–61]</sup> are not significant in the C1s region. The O1s region shows a strong response at binding energies > 534 eV at all SEIs, thus indicating the presence of alkyllic species. O1s regions show no presence of Li<sub>2</sub>O, though indicate the presence of Li<sub>2</sub>CO<sub>3</sub> in both lower potential SEIs. The higher potential SEIs show no signs of Li<sub>2</sub>CO<sub>3</sub>. The F1s region indicates the presence of LiF and residual LiPF<sub>6</sub> in all SEIs, while the 450 mV SEI exhibits higher fluorophosphate content. Figure 2 also shows the elemental percentages of oxygen and fluorine normalized with the carbon concentration for the different

formation potentials. The oxygen content suggests two distinct regimes: “low-potential” (< 400 mV) and “high-potential” (> 400 mV) SEIs, where the high-potential SEIs contain about twice as much oxygen as the low-potential ones, whereas only the latter exhibit carbonate features. Though, no trend is present in the fluorine content with formation potential. Nevertheless, the absolute values < 10% indicate all fluorine containing species to be present only in small amounts. Apart from residual LiPF<sub>6</sub>, we tentatively attribute these fluorine concentrations to thin, non-passivating LiF films formed via HF reduction. We recently demonstrated, that such films form at potentials > 1 V,<sup>[40]</sup> and that their formation requires electrocatalytically active sites, of which HOPG has few. Hence our formation potential should have little influence on them, so that no trend was to be expected in the first place.

In summary, the XPS measurements confirm an influence of the formation potential on the SEI chemistry. Most obvious is the apparent segregation into a high (600 and 450 mV) and a low (300 and 100 mV) potential regime resulting in absence/presence of Li<sub>2</sub>CO<sub>3</sub> and high/low oxygen concentrations, respectively. Hence, on HOPG, the frequently assumed direct decomposition of EC to Li<sub>2</sub>CO<sub>3</sub> and ethylene – if at all – only takes place at < 400 mV (in agreement with Aurbach et al.).<sup>[62]</sup>

## 2.3. Electrochemical Investigations

### 2.3.1. Cyclic Voltammetry

We used cyclic voltammetry to investigate the electron and species transport properties of the different SEIs. Fc/Fc<sup>+</sup> served as a stable probe species in the absence of intercalating Li on HOPG.<sup>[63]</sup> The use of Li<sup>0</sup> reference and counter electrode is appropriate, since Fc/Fc<sup>+</sup> shows good chemical stability at low potentials.<sup>[64,65]</sup> We injected Fc/Fc<sup>+</sup> enriched electrolyte after SEI

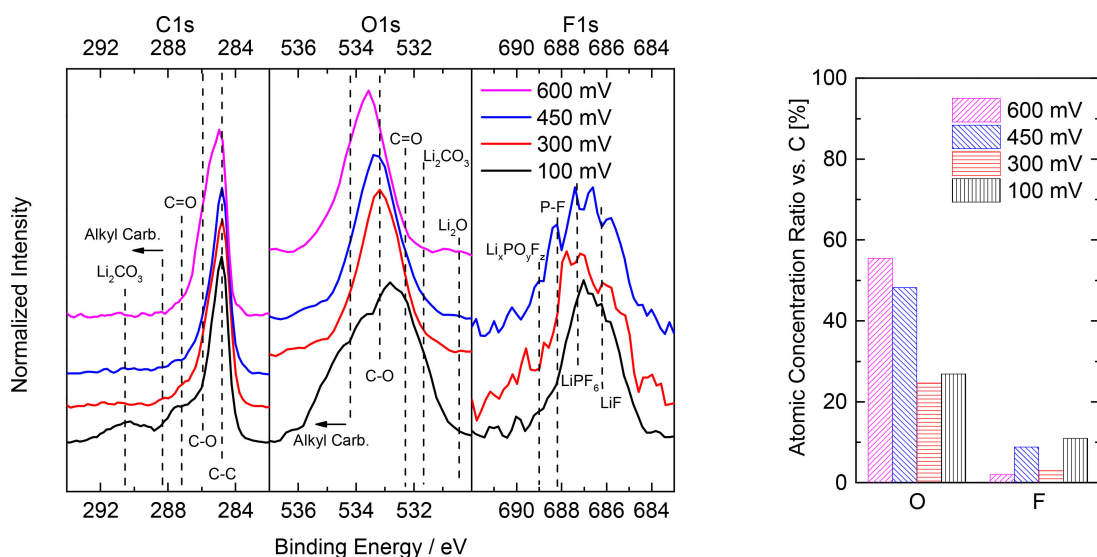


**Figure 2.** XPS C1s, O1s and F1s spectra (left) and elemental concentrations (right) for SEIs formed at indicated potentials. Dashed lines mark standard SEI species bindings at respective binding energies. The 600 mV SEI did not show any significant counts in the F1s region. The concentrations are given as a ratio vs. carbon.

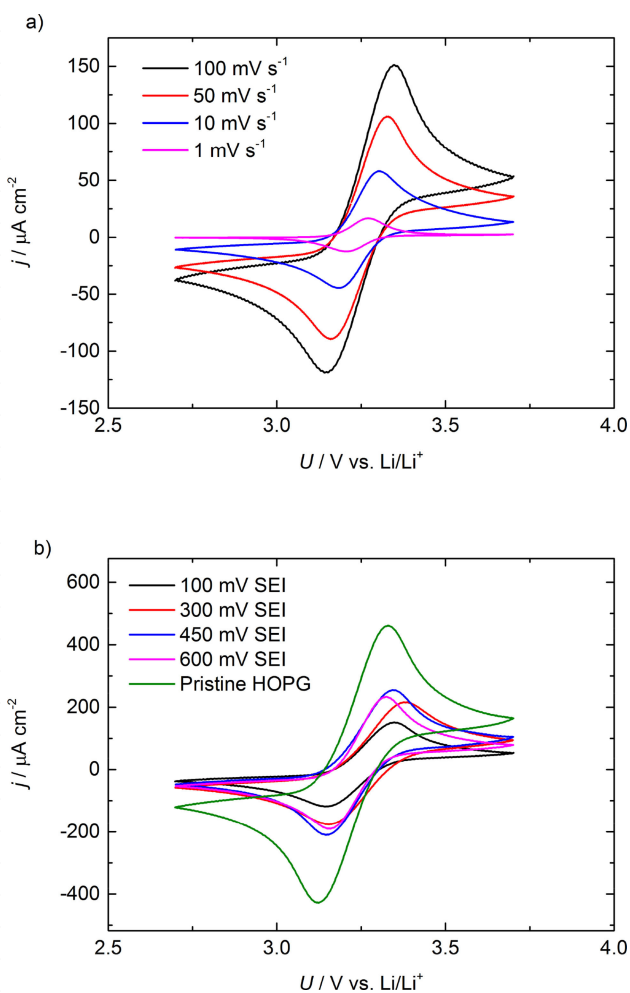


**Figure 3.** CVs of HOPG covered by SEIs Fc/Fc<sup>+</sup> environment. For every scan rate 5 cycles were obtained, only the fifth is shown. a) CVs with different scan rates of an SEI formed at 100 mV. b) CVs at 100 mVs<sup>-1</sup> on pristine HOPG and different SEIs.

formation. To ensure sufficient equilibration we obtained 5 cycles per scan rate and only used the respective 5<sup>th</sup> cycle for further analysis and comparison. Figure 3a exemplarily shows the data of a 100 mV SEI (trends of CVs on different SEI are similar). Figure 3b presents the CVs on different SEIs as well as pristine HOPG obtained at 100 mVs<sup>-1</sup>. The shapes generally indicate a fully reversible reaction. The peak current densities are up to two orders of magnitude higher than the current densities in neat electrolyte (see SI) and 1.5 orders of magnitude higher than the passivation currents at the end of the formation procedure (Figure 1c), confirming that any background currents can be neglected in the presence of the Fc/Fc<sup>+</sup> couple. The current densities are consistent with previous findings for other solvent/electrode systems.<sup>[63,66–68]</sup>

With decreasing scan rate, the peaks get smaller (Figure 3a), as expected. However, the peak positions are not constant for the different scan rates. This indicates that the underlying processes are more complex than a Nernstian uninhibited behavior.

Comparing the CVs obtained after different formation potentials (Figure 3b), the CVs qualitatively retain the same characteristic shape, but become smaller in amplitude in the presence of an SEI. The suppression is strongest for the 100 mV SEI, whereas SEIs formed at any of the three other formation potentials yield rather similar CV amplitudes. Another obvious feature is the shift of the peak potentials, which does not seem to follow any specific trend. These latter shifts highlight that the SEI does more than just block parts of the electrochemically active surface area (ECSA) and obstruct the diffusion transport of Fc/Fc<sup>+</sup>. This is discussed in more detail in the SI, where we demonstrate that CV simulations only resemble the experimental trends if we not only allow for a variation of the ECSA and the effective diffusion coefficients, but also of the kinetic rate constant for the redox reaction.

In the following, we will derive the (apparent) diffusion coefficients and heterogeneous rate constants from the trends in CV peak amplitudes and positions, respectively.

**Diffusion coefficients from peak amplitudes.** For a given SEI, information about how diffusion transport of Fc/Fc<sup>+</sup> is hindered by the SEI can be determined from the scan-rate dependent peak amplitude.<sup>[69]</sup> The anodic peak current densities  $j_{\text{peak}}$  of different SEIs as well as pristine HOPG plotted against the square root of the scan rate  $\nu$  are shown in Figure 4a. One can observe a linear dependency of the peak current densities with  $\nu^{1/2}$ , confirming the quasi-reversibility of the Fc/Fc<sup>+</sup> reaction even in the presence of an SEI.<sup>[69–71]</sup> For quasi-reversible reactions, the oxidative peak current density  $j_{\text{peak}}$  depends on the scan rate and is described at 20 °C by the adjusted Randles-Sevcik equation [Eq. (1)]:<sup>[69]</sup>

$$j_{\text{peak}} = 3.04 \cdot 10^5 n^{3/2} \alpha^{1/2} c_{\text{Red}}^0 (\xi D_{\text{red}} \nu)^{1/2} \text{ in A cm}^{-2} \quad (1)$$

$D_{\text{red}}$  = effective diffusion coefficient (reduced species) = to be determined,  $n$  = transfer number = 1,  $\alpha$  = charge transfer coefficient = 0.3,<sup>[72]</sup>  $c_{\text{Red}}^0$  = concentration (reduces species) = 2.5 mMol, respectively. The correction factor  $\xi$  is equal 1 for solutions where the oxidized species concentration  $c_{\text{ox}}^0$  respects the boundary conditions  $c_{\text{ox}}^0(t=0) = c_{\text{ox}}^0(x \rightarrow \infty) = 0$ . Since in our experiments we started with a non-zero concentration of the oxidized species,  $\xi$  must be derived from another method. By comparison with EIS measurements (see SI), we find  $\xi = 3.97$ . Data is fitted using linear fits with y-intercepts equal zero. The slope is significantly higher on pristine HOPG and decreases with lowered formation potential, indicating a reduced effective diffusion coefficient. The slopes of the 100 mV SEI is distinctly smaller, whilst the other three SEIs seem to have similar diffusion properties. The analysis of the reductive peak currents leads to similar slopes, therefore they are not discussed separately (see also Dinh-Nguyen et al.<sup>[39]</sup>). Though, they allow the conclusion that the oxidized and reduced species effective diffusion coefficients  $D_{\text{ox}}$  and  $D_{\text{red}}$  are similar too. The corresponding fit slopes as well as the resulting effective diffusion coefficients  $D_{\text{eff}} = D_{\text{red}} \approx D_{\text{ox}}$ , calculated using [Eq. (1)], are presented in Table 1.

The strong drop of diffusion coefficient between 300 and 100 mV resembles well the glassy carbon rotating disk

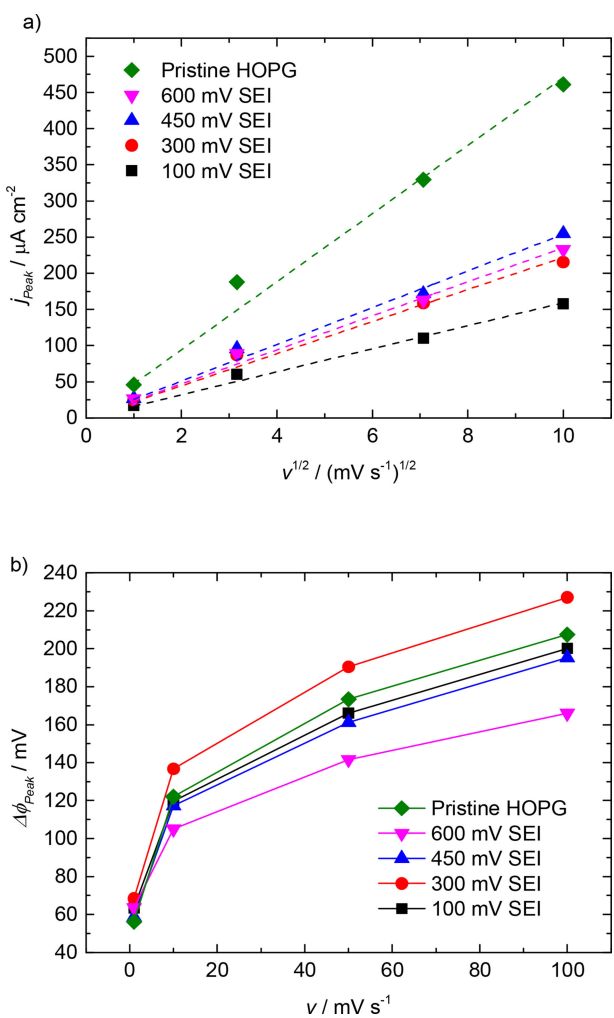


**Figure 4.** a) CV anodic peak current densities  $j_{\text{peak}}$  obtained on pristine HOPG and different SEIs in  $\text{Fc}/\text{Fc}^+$  environment plotted vs.  $v^{1/2}$  and respective linear fits (dashed lines) for diffusion coefficient calculations. b) Peak potential differences  $\Delta\varphi_{\text{peak}}$  of CVs obtained on pristine HOPG and different SEIs in  $\text{Fc}/\text{Fc}^+$  environment.

electrode (GC-RDE) limiting current results by Tang et al.<sup>[23]</sup> Interestingly, that paper has another set of data which – when analyzed appropriately – is also in good agreement with our diffusion coefficients. Figure 5a reproduces a figure of ref.<sup>[23]</sup>, which shows the OCP transient of SEI covered GC-RDE during  $\text{Fc}/\text{Fc}^+$  injection. SEIs were formed at indicated potentials in a similar way to our study. We reprocessed that data by shifting the moment of injection (arrows in Figure 5a) to  $t = 0.1$  s and present the reprocessed data in Figure 5b. Since the OCP is

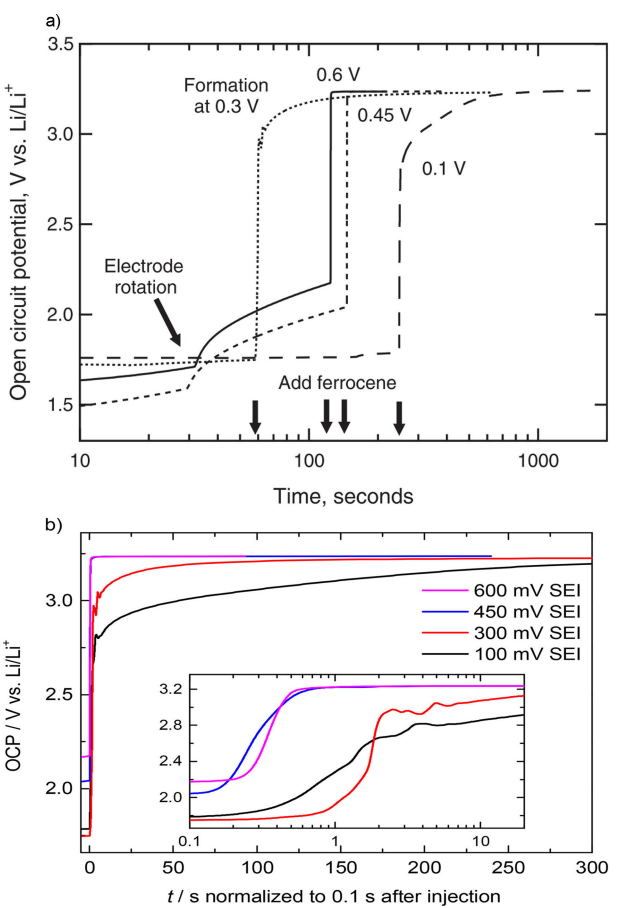


**Figure 5.** a) OCP transients after injection of  $\text{Fc}/\text{Fc}^+$  in different SEIs on Glassy Carbon in a RDE system (reproduced from ref.<sup>[23]</sup>; Journal of the Electrochemical Society by Electrochemical Society. Reproduced with permission of Electrochemical Society in the format/magazine via Copyright Clearance Center). b) Same data reprocessed by shifting the moment of injection to  $t = 0.1$  s. Inset presents data with logarithmic time axis for better visibility of the initial phases.

directly correlated to the  $\text{Fc}/\text{Fc}^+$  concentration at the electrode, the OCP slope and thus the time to reach a selected potential are qualitative measures for the  $\text{Fc}/\text{Fc}^+$  diffusion speed. The durations for the OCP to reach 3.1 V are 0.46, 0.49, 14 and 142 s for the 600, 450, 300 and 100 mV SEI, respectively. That trend is fully compatible with the diffusion coefficients in Table 1.

**Heterogeneous rate constants from peak potentials.** The peak potential differences in Figure 4b generally decrease with lowered scan rate and approach the theoretical value of 57 mV for a fully reversible system.<sup>[71]</sup> Though, without an appropriate discussion of the electrochemical background, the dependency

**Table 1.** Electrochemical results extracted from CVs or calculated using equations (1) and (2).

	Slope $j_{\text{peak}}$ vs. $v^{1/2}$ $10^{-4} \text{ A cm}^{-2} (\text{V s}^{-1})^{-1/2}$	$D_{\text{eff}}$ $10^{-6} \text{ cm}^2 \text{s}^{-1}$	$A_{50}$	$k_{0,50}$ $10^{-4} \text{ cm s}^{-1}$	$A_{10}$	$k_{0,10}$ $10^{-4} \text{ cm s}^{-1}$
Pristine HOPG	15	3.2	0.32	8.1	0.61	6.9
600 mV SEI	7.4	0.80	0.44	5.6	0.89	5.0
450 mV SEI	8.0	0.93	0.36	4.9	0.68	4.1
300 mV SEI	7.0	0.72	0.26	3.1	0.48	2.6
100 mV SEI	5.0	0.37	0.35	3.0	0.64	2.4

trend of the peak potential difference on the SEI formation potential appears to be rather random. As it was described by Matsuda and Ayabe, the heterogeneous rate constant  $k_0$  of a quasi-reversible reaction can be determined from the peak potential difference as well as the effective diffusion coefficient [Eq. (2)]:<sup>[69]</sup>

$$k_{0,\nu} = A_\nu(\Delta\varphi_{Peak}) \cdot \left( D_{eff} \frac{nF}{RT} \nu \right)^{1/2} \quad (2)$$

where  $F$  is the Faraday constant and  $R$  the universal gas constant.  $A_\nu(\Delta\varphi_{Peak})$  is a numerical function of which a set of values is tabulated in the literature.<sup>[71]</sup> In theory,  $k_0$  is independent of  $\nu$ , though values based on experimental data can vary with scan rate, therefore the index  $\nu$  is used to indicate the respective scan rate. The  $k_{0,\nu}$  values listed in Table 1 are calculated with [Eq. (2)] by using  $A_\nu$  values interpolated from the tabulated data in order to derive rate constants for 50 and 10 mVs<sup>-1</sup>. The peak potential differences of 100 and 1 mVs<sup>-1</sup> are outside the tabulated  $A_\nu$  interval and can therefore not be considered. Although diffusion coefficients determined in ref.<sup>[72]</sup> on glassy carbon vary significantly, rate constants of pristine HOPG are consistent with values derived in the corresponding glassy carbon experiments. The calculated rate constants in Table 1 slightly depend on the respective  $\nu$ . Consistent with our XPS results, a much more pronounced difference can be

observed between the high (600 and 450 mV) and the low (300 and 100 mV) formation potentials regimes. Although the peak potential differences did not reveal any trend with formation potential at first, a clear trend emerges for the heterogeneous rate constants of the Fc/Fc<sup>+</sup> outer sphere reaction whose calculations using [Eq. (2)] include the effective diffusion coefficients. Hence the formation potential not only changes the SEI's transport properties for the probe species to reach the electrochemically active interface, but also the kinetics of the electrochemical reaction itself.

### 2.3.2. Electrochemical Impedance Spectroscopy

In order to widen the understanding of the individual electrochemical features and their activation energies and to obtain ionic movement coefficients, low and high-potential SEIs were investigated using EIS. As representatives, we considered 450 and 300 mV as lowest/highest potential of the high/low formation potential regime, respectively. The characteristics of SEIs formed at those two potentials differ significantly, yet the two potentials are very close to each other. This underlines the "step" characteristics of the changes between the two regimes. Figure 6 shows the Nyquist plots and the Distribution of Relaxation Times (DRT)  $g(f)$ , the latter calculated following the scheme from refs<sup>[73]</sup> and<sup>[74]</sup>  $g(f)$  is presented only in the regions

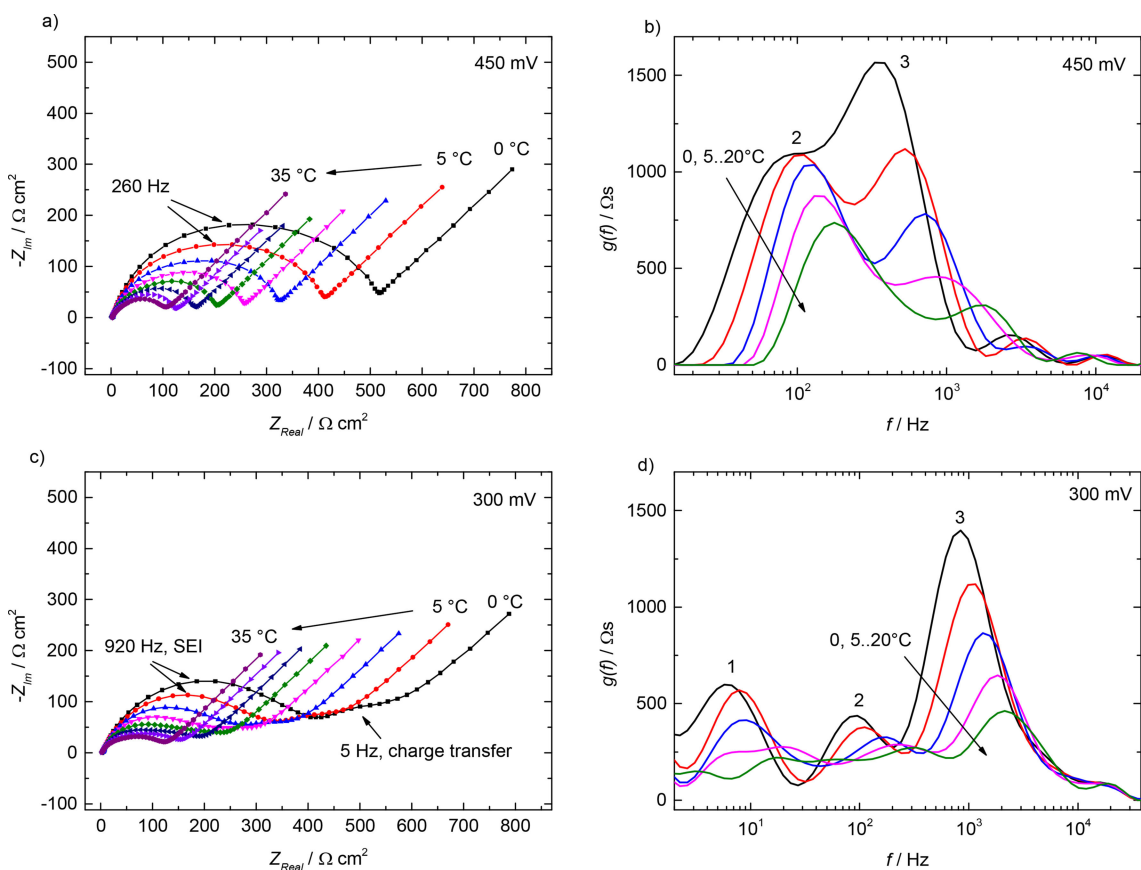


**Figure 6.** a) and b) Temperature dependent impedance spectra of a high-potential SEI (450 mV) in Fc/Fc<sup>+</sup> environment presented as Nyquist and DRT plots. c) and d) Respective impedance spectra of a low-potential SEI (300 mV) presented as Nyquist and DRT plots.

where both real and imaginary residuals are reasonably small. The DRT plots of all temperatures, DRT residuals and Bode phase plots can be found in the SI. The spectra were recorded around OCP at 5 K steps starting from 0 °C up to 35 °C as indicated by the arrows, though for better illustration DRT slopes above 20 °C are not shown. The OCP remained constant in the entire temperature interval at ~3.23 V. The high frequency intercepts decrease with rising temperature from 5 Ω cm<sup>2</sup> down to 2.5 Ω cm<sup>2</sup>, which can be assigned to the variation of the electrolyte bulk conductivity.<sup>[75]</sup>

The high-potential SEI in Figure 6a and b exhibits the following features: The Nyquist plots consist of a single distorted semicircle in the whole temperature interval. DRT plots in the shown frequency region show two broad overlapping peaks assigned as numbers 2 and 3. The frequency at the Nyquist semicircle maximum is at 260 Hz (indicated by the arrow), which lies in between the two DRT peak maxima. As discussed in detail in the SI, DRT peak 3 shifts faster with rising temperature. The distortion of the Nyquist plot and the width of the DRT peaks both indicate the existence of two scattered features with different activation energies. This implies that SEIs cannot be sufficiently modeled with simple RC-containing equivalent circuits. Respective attempts usually lead to good simulation fits, though lack of physical meaning (e.g. Levi et al. used several RC-elements<sup>[76]</sup>).

For the low-potential SEI, temperature dependent Nyquist and DRT plots (Figure 6c and d) show more features than for the high-potential SEI. Nyquist plots consist of a large distorted semicircle at high frequencies, followed by a small distorted semicircle in the low frequency region. The smaller semicircle disappears with rising temperature. It is common to assign low frequency semicircles to the Li/Li<sup>+</sup> charge transfer process, whilst high frequency semicircles are related to the ion migration through the SEI.<sup>[18,58,77,78]</sup> Although the charge transfer in the system was Fc/Fc<sup>+</sup> instead of Li/Li<sup>+</sup>, the two distorted semicircles will be referred to as SEI and charge transfer semicircle, respectively. The low frequency charge transfer semicircle shows a corresponding peak in the DRT plot at ~5 Hz assigned as peak 1. The Nyquist maximum at around 920 Hz corresponds nicely with DRT peak 3. DRT peak 2 frequencies resemble almost the values from the DRT analysis of the high-potential SEI in Figure 6b. Both charge transfer and SEI impedances in the Nyquist plot decrease with increasing temperature, as obvious from the shrinking semicircles, particularly the disappearing charge transfer semicircle in Figure 6c as well as the DRT peak shift towards higher regions in Figure 6d. We attribute this movement characteristics to mechanism-specific activation energies, which we discuss in more detail in the SI.

For both SEIs, the DRT peaks are rather broad. On porous electrodes, such peak broadening is caused by through-plane distributions,<sup>[73]</sup> whereas on a flat electrode like HOPG we tentatively assign it laterally inhomogeneous surface layer properties.

Both kinds of SEIs share the high frequency SEI Nyquist semicircle as a common feature with a similar total ohmic resistance. In the DRT picture, this is reflected in similar peaks 2

and 3, while the low-potential SEI includes another charge transfer feature (DRT peak 1). In both Nyquist and DRT plots the charge-transfer related features can only be separated from migration (high frequency) and diffusion (low frequency) when the charge transfer itself becomes slower, i.e., kinetically more hindered. That is only the case for the low-potential SEI (Figure 6c and d) and only at lower temperatures. The fact that it becomes distinguishable at all, however, is an important indicator that the formation potential does not only influence the porosity and tortuosity (influence on ion migration and diffusion) but also hinders the reaction kinetics (consistent with CV rate constants in Table 1). Therefore, the slightly broader high frequency response of the 450 mV SEI in both Nyquist and DRT plots (Figure 6a and b) is not to be confused with the actual Fc/Fc<sup>+</sup> migration impedance as it probably includes the respective charge transfer contribution (DRT peak 1).

EIS allowed the distinct separation of two mechanisms, the ionic movement and the charge transfer. In the SI we analyze the temperature dependency of the two kinds of SEIs and calculate activation energies of charge transfer and ionic movement. The activation energies for diffusion and migration of Fc/Fc<sup>+</sup> are significantly smaller than the value for charge transfer, indicating that electrons have to overcome significant energy barriers, with notable effects in particular at low temperatures. Furthermore, EIS showed that ionic movement is similar in the different SEIs, while the charge transfer is significantly more hindered in the presence of low-potential SEIs as compared to high-potential SEIs. Although EIS addresses completely different physical parameters, results qualitatively replicate the findings from CV experiments.

## 2.4. Discussion

We discuss our findings in the framework of the simplified two-layer model of the SEI, best represented by this sequence electrode|SEI (compact layer)|SEI (porous layer)|electrolyte. This neglects lateral inhomogeneities and reduces the SEI to a thin compact layer at the electrode surface and a significantly thicker porous layer on the electrolyte side (see Figure 7). The compact layer is quasi solid and Li<sup>+</sup> conductive, while the porous layer is soaked with electrolyte. The desolvation of Li<sup>+</sup>

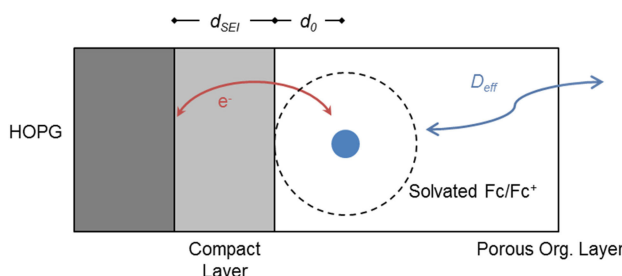


**Figure 7.** Proposed reaction mechanism of Fc/Fc<sup>+</sup> at HOPG covered by an SEI. The electrons must tunnel through the insulating and impermeable compact layer leading to an additional exponential term in the rate constant of the outer sphere reaction. The diffusion/migration limitation is determined by the outer porous layer mainly consisting of organic compounds.

takes place at the interface between compact and porous layer.<sup>[36,37,55–57,79–83]</sup> Inorganic species like Li<sub>2</sub>CO<sub>3</sub> are believed to arise close to the electrode surface, while porous organic species are usually accumulated at the electrolyte side.<sup>[22,55,56,84,85]</sup> We suggest that SEI formation on HOPG splits into the following steps, which will be justified in this chapter.

> 700 mV	Only negligible electrolyte reduction without an insulating surface coverage. The formed species are soluble and stripped off when re-increasing the potential.
First Step: ~700 mV	Formation of a porous long-chained organic interphase affecting ionic movement properties. <b>Thin electronically insulating organic compact layer</b> on the surface passivates further electrolyte reduction.
Second Step: ~400 mV	<b>Reduction of pre-formed organic compact SEI forms thicker inorganic compact SEI</b> at electrode surface. Shortening of organic chains leads to further reduces effective diffusion coefficient in porous layer.

Starting with the compact layer: it is the substantial passivation factor, since it is supposed to be impermeable and electronically insulating. While all investigated SEIs in this work are passivating towards further electrolyte reduction, XPS results point out differences by means of elemental concentrations, in particular Li<sub>2</sub>CO<sub>3</sub> existence. Therefore, although passivating, the high-potential compact layer must consist of organic species. On the other hand, XPS showed significant amounts of inorganic species in low-potential SEIs, which consequently must be formed via reduction of the pre-formed organic compact layer. This is in agreement with the findings of both Matsouka et al. and Tang et al., who found CV reduction peaks at high potentials only in the first cycle, while the subsequent cycles included only the second (low-potential) reduction peak.<sup>[29,35]</sup>

**Effective tunneling thickness of the compact layer.** Obviously, the presence and kind of a passivated SEI affects the kinetics though does not fully inhibit the Fc/Fc<sup>+</sup> reaction. The trend in reaction rate constant  $k_{0,v}$  shown in Table 1 invites for a quantitative discussion of the Fc/Fc<sup>+</sup> reaction kinetics. The kinetics are strongly correlated to the formation potential, which allows us excluding two hypotheses: Neither is the SEI re-oxidized or becomes conductive at ~3.2 V (where the Fc/Fc<sup>+</sup> experiments were performed), nor is Fc/Fc<sup>+</sup> able to migrate or diffuse to the electrode surface. Otherwise we would have expected formation potential independent kinetics. Thus, independent of their chemical properties, the compact layer microphases proposed by Peled et al.<sup>[85]</sup> must be attached tightly so that the compact layer cannot be penetrated by the Fc/Fc<sup>+</sup> species. We support the hypothesis that electrons tunnel through the passivated SEI to react with Fc/Fc<sup>+</sup>.<sup>[30,86]</sup> Since the porous layer is soaked with electrolyte, the tunneling

takes place through the compact layer. The proposed total reaction mechanism is schematically shown in Figure 7.

Fc/Fc<sup>+</sup> is known to have an outer-sphere reaction, at which the electrons have to tunnel through a shell surrounding the electrochemical active center.<sup>[87,88]</sup> If the shell radius being the minimum tunneling distance is described as  $d_0$ , in accordance with the Marcus theory the reaction rate constant  $k_0$  on pristine HOPG is directly proportional to  $\exp(-\gamma d_0)$ .  $\gamma > 0$  describes the tunneling probability and depends among others on the tunneling energy barrier.

Assuming that the compact SEI layer does nothing more than adding a further tunneling barrier with a thickness  $d_{SEI}$  and a tunneling probability  $\beta > 0$ , we get Equation (3) for the rate constant proportionality on SEI covered HOPG:

$$k_0 \propto \exp(-\gamma d_0 - \beta d_{SEI}) \quad (3)$$

The rate constant calculated for pristine HOPG,  $k_0^{Pristine}$ , corresponds to the special case where  $d_{SEI} = 0$ . It actually provides the proportionality constant between the rate constant of an SEI covered sample and the compact layer thickness [Eq. (4) and (5)]:

$$k_0 = k_0^{Pristine} \exp(-\beta d_{SEI}) \quad (4)$$

$$\Rightarrow d_{SEI} = -\frac{1}{\beta} \ln\left(\frac{k_0}{k_0^{Pristine}}\right) \text{ with } k_0 \leq k_0^{Pristine} \quad (5)$$

The factor  $\beta$  could not be determined in this study. Table 2 shows the resulting  $\beta d_{SEI,v}$  calculated from  $k_{0,v}$  values from Table 1.  $\beta$  should mainly depend on the energy levels of the

**Table 2.** SEI thicknesses calculated using [Eq. (5)] resulting from CVs at 50 and 10 mV s<sup>-1</sup>. The factor  $\beta$  could not be determined experimentally, though can be assumed to be invariant.

	600 mV	450 mV	300 mV	100 mV
$\beta \cdot d_{SEI,50}$	0.38	0.50	0.96	1.0
$\beta \cdot d_{SEI,10}$	0.32	0.51	0.99	1.0

tunneling barrier neighborhood, therefore we assume  $\beta$  invariant. Thus, the presented “thicknesses” can be directly compared. Although the SEI thicknesses of the 600 and 450 mV SEIs differ slightly, the switchover to the low-potentials doubles the calculated compact layer thickness. The 450 mV, although being an edge potential before the second formation step, might thermodynamically already enable second step reactions in small rates.<sup>[35]</sup> This would be consistent with a slightly thicker compact layer of the 450 mV SEI as compared to the 600 mV SEI. We would also like to mention that a possibly incorrectly defined Randles-Sevcik correction factor  $\xi$  in [Eq. (1)] would have no effect on these thickness values as  $\xi$  becomes obsolete in [Eq. (5)].

**Evolution of Transport Properties.** Particular attention also needs to be paid on the Fc/Fc<sup>+</sup> transport properties, which are defined by the outer porous layer that mainly consist of organic compounds. The diffusion coefficient (Table 1) is reduced significantly during the first formation step (at ~700 mV). The

further reduction between the 300 and 100 mV SEI could be caused by a reaction at  $\sim 400$  mV, which though is sluggish and demands a high overpotential to be activated (not sufficiently given at 300 mV). One may speculate, that the reaction step could consist of a shortening of the long chained organic molecules in the porous layer. The resulting changes affect the SEI adsorption properties, which lead to the change in diffusion activation energies (presented in SI).<sup>[89]</sup> The intrinsic diffusion coefficient is assumed to not be affected by the presence of surface layers. In agreement with Tang et al., we suggest, that the shorter polymer chains form a tighter and less porous layer with higher tortuosity and a reduced effective diffusion coefficient.<sup>[37]</sup> This hypothesis was also studied in more detail and will be in the focus of a future publication.<sup>[90]</sup>

**Transferability to commercial electrode material.** It is important to mention that both the obtained trends in kinetics and transport properties of  $\text{Fc}/\text{Fc}^+$  are not necessarily transferable to  $\text{Li}^+$ .<sup>[91]</sup> E.g. the trend in effective diffusion coefficient is not expected to be relevant, since the actual transport limitations are given by the  $\text{Li}^+$  migration through compact inorganic layer (which we consider impermeable for  $\text{Fc}/\text{Fc}^+$ ). On the other hand,  $\text{Li}^+$  intercalation rate constant is not determined by surface layers, but by other properties like the  $\text{Li}^+$  desolvation and the ratio of graphite surface orientation.<sup>[31,78]</sup> Though, the ability of  $\text{Fc}/\text{Fc}^+$  to react via a tunneling is believed to be also possible for other transition metal cations like  $\text{Mn}^{2+}$  (particularly under those high driving forces: overpotentials  $> 1$  V), which is important for longer-term cell degradation by side reactions like ongoing SEI growth.

In our study we could show that, on HOPG, the low-potential compact SEI is a product of high-potential SEI decomposition. Thus, having in mind commercial composite electrodes, the "optimal" reaction conditions of the two reaction steps might differ significantly. We believe that particularly the second step, which is located in the potential operation region of anodes, is crucial for the stability as well as physicochemical properties of the final SEI. On the other hand, since the second step reactions depend on the quantity and quality of the high-potential SEI, formation protocols should be optimized also in terms of improving the high-potential SEI properties. A first study validating this assumption was recently published by our group.<sup>[92]</sup>

### 3. Conclusions

HOPG was used to study SEI formation at potentiostatic conditions, which are achievable without strong cell polarization due to the low surface area of this sample. Furthermore, the basal plane of HOPG is chemically inert, and  $\text{Li}^+$  intercalation is negligible. We studied SEIs formed at four different potentials (600, 450, 300, 100 mV), analyzing their chemical composition by ex-situ XPS and their electrochemical (transport) properties through the interaction with  $\text{Fc}/\text{Fc}^+$  as a probe species.

SEI formation is found self-terminating, hence self-passivating at all potentials investigated, which implies the formation

of an electronically insulating layer, which is also impermeable for SEI-forming electrolyte components (thus: compact layer). XPS revealed  $\text{Li}_2\text{CO}_3$  formation only for the two lower formation potentials (300 and 100 mV), i.e. the high-potential compact SEI is essentially organic. This also shows that, contrary to prevalent opinion, carbonate formation is not necessary for electrode passivation. The SEI formation process in commercial cells makes use of galvanostatic conditions, which leads to a slow potential sweep from higher to lower potentials. Given that our results indicate a suppression of direct electrochemical electrolyte decomposition already by the high-potential SEI, we conclude that the typical carbonate layers found after such galvanostatic SEI formation, which is performed at least down to  $\text{Li}^+$  intercalation potentials ( $< 220$  mV vs.  $\text{Li}/\text{Li}^+$ ), result from further electrochemical decomposition of the pre-formed high-potential organic compact SEI.

The presence of a compact SEI after formation is also confirmed by  $\text{Fc}/\text{Fc}^+$  cyclic voltammetry and corresponding EIS experiments. For all four potentials, those measurements revealed significant inhibition of charge transfer kinetics through the SEIs as compared to pristine HOPG. In agreement with the XPS observation of carbonate only for the low-potential (300 and 100 mV) SEIs, we also find that the latter exhibit much more sluggish electron transfer kinetics than the high-potential (600 and 450 mV) SEIs. Based on a simple electron tunneling model, these observations allowed us to calculate the factors by which the effective tunneling distances change, which we tentatively associate with the thicknesses of the compact SEIs.

As a side result, the CV and EIS data also reveal some information about the ionic movement (migration and diffusion) through the outer part of the SEI, the porous layer: effective permeability is found to decrease with decreasing formation potential, which we tentatively assign to a shortening of the organic polymer chains formed from ring-opening reactions of ethylene and vinylene carbonate.

In summary, the previously described two-step process of SEI formation would start at  $\sim 700$  mV with the formation of an organic compact layer (covered by a porous one), which is then itself reduced to a much thicker compact, yet inorganic (carbonate containing) layer once potentials drop (either in a CV or due to galvanostatic control) to below  $\sim 400$  mV. Knowing that, we conclude that by controlling the chemical and physical properties of the high-potential SEI, one can significantly influence the respective properties of the final low-potential SEI and thus influence the lifetime and conductivity properties of SEIs in commercial cells.

### Acknowledgements

We gratefully acknowledge the fruitful discussions with Stefan Klink and Giorgia Zampardi (formerly RU Bochum) on the stability of ferrocene complexes, with Sebastian Keller (BMW Group) on the Laplace transformation and with Kevin Leung (Sandia National Lab) on the theoretical perspectives. This work was carried out

with funding from the Faraday Institution ([faraday.ac.uk](http://faraday.ac.uk); EP/S003053/1), grant number FIRG003.

## Conflict of Interest

The authors declare no conflict of interest.

**Keywords:** electrochemistry • highly oriented pyrolytic graphite • model electrode surface • materials science • outer sphere reaction

- [1] M. Winter, W. K. Appel, B. Evers, T. Hodal, K.-C. Möller, I. Schneider, M. Wachtler, M. R. Wagner, G. H. Wrodnigg, J. O. Besenhard, *Monatsh. Chem.* **2001**, *132*, 473–486
- [2] J. Vetter, P. Novak, Wagner, C. Veit, K.-C. Möller, J. O. Besenhard, M. Winter, M. Wohlfahrt-Mehrens, C. Vogler, A. Hammouche, *J. Power Sources* **2005**, *147*, 269–281
- [3] D. P. Abraham, J. L. Knuth, D. W. Dees, I. Bloom, J. P. Christoffersen, *J. Power Sources* **2007**, *170*, 465–475
- [4] Y. Ein-Eli, B. Markovsky, D. Aurbach, Y. Carmeli, H. Yamin, S. Luski, *Electrochim. Acta* **1994**, *39*, 2559–2569
- [5] D. Andre, S.-J. Kim, P. Lamp, S. F. Lux, F. Maglia, O. Paschos, B. Stiaszny, *J. Mater. Chem. A* **2015**, *3*, 6709–6732
- [6] Y. Li, M. Bettge, B. Polzin, Y. Zhu, M. Balasubramanian, D. P. Abraham, *J. Electrochem. Soc.* **2013**, *160*, A3006–A3019
- [7] D. Aurbach, E. Zinigrad, Y. Cohen, H. Teller, *Solid State Ionics* **2002**, *148*, 405–416
- [8] P. Verma, P. Maire, P. Novak, *Electrochim. Acta* **2010**, *55*, 6332–6341
- [9] M. B. Pinson, M. Z. Bazant, *J. Electrochem. Soc.* **2013**, *160*, A243–A250
- [10] J.-Y. Eom, I.-H. Jung, J.-H. Lee, *J. Power Sources* **2011**, *196*, 9810–9814
- [11] H. Ota, Y. Sakata, A. Inoue, S. Yamaguchi, *J. Electrochem. Soc.* **2004**, *151*, A1659–A1669
- [12] B. Stiaszny, J. C. Ziegler, E. E. Krauß, J. P. Schmidt, E. Ivers-Tiffée, *J. Power Sources* **2014**, *251*, 439–450
- [13] M. Zhou, L. Zhao, S. Okada, J.-i. Yamaki, *J. Electrochem. Soc.* **2011**, *159*, A44–A48
- [14] D. Aurbach, A. Zaban, Y. Ein-Eli, I. Weissman, O. Chusid, B. Markovsky, M. Levi, E. Levi, A. Schechter, E. Granot, *J. Power Sources* **1997**, *68*, 91–98
- [15] E. Peled, D. Golodnitsky, C. Menachem, D. Bar-Tow, *J. Electrochem. Soc.* **1998**, *145*, 3482–3486
- [16] A. Schechter, D. Aurbach, H. Cohen, *Langmuir* **1999**, *15*, 3334–3342
- [17] S. S. Zhang, K. Xu, T. R. Jow, *Electrochim. Acta* **2004**, *49*, 1057–1061
- [18] D. Aurbach, K. Gamolsky, B. Markovsky, Y. Gofer, M. Schmidt, U. Heider, *Electrochim. Acta* **2002**, *47*, 1423–1439
- [19] W. Märkle, C.-Y. Lu, P. Novak, *J. Electrochem. Soc.* **2011**, *158*, A1478–A1482
- [20] E. Peled, D. Bar Tow, A. Merson, A. Gladkikh, L. Burstein, D. Golodnitsky, *J. Power Sources* **2001**, *97*, 52–57
- [21] E. Peled, D. Golodnitsky, A. Ulus, V. Yufit, *Electrochim. Acta* **2004**, *50*, 391–395
- [22] D. Aurbach, *J. Power Sources* **2000**, *89*, 206–218
- [23] M. Tang, S. Lu, J. Newman, *J. Electrochem. Soc.* **2012**, *159*, A1775–A1785
- [24] S. Zhang, M. S. Ding, K. Xu, J. Allen, T. R. Jow, *Electrochim. Solid-State Lett.* **2001**, *4*, A206–A208
- [25] M. P. Mercer, H. E. Hoster, *Nano Energy* **2016**, *29*, 394–413
- [26] N. M. Markovic, *Surf. Sci. Rep.* **2002**, *45*, 117–229
- [27] D. Bar-Tow, E. Peled, L. Burstein, *J. Electrochem. Soc.* **1999**, *146*, 824–832
- [28] J. Ma, L. Seidl, W. Ju, E. Mostafa, L. Asen, S. Martens, U. Stimming, O. Schneider, *ECS Trans.* **2014**, *64*, 407–423
- [29] M. Tang, K. Miyazaki, T. Abe, J. Newman, *J. Electrochem. Soc.* **2012**, *159*, A634–A641
- [30] M. Tang, J. Newman, *J. Electrochem. Soc.* **2012**, *159*, A1922–A1927
- [31] Y. Yamada, Y. Iriyama, T. Abe, Z. Ogumi, *Langmuir* **2009**, *25*, 12766–12770
- [32] Y. Domi, M. Ochida, S. Tsubouchi, H. Nakagawa, T. Yamanaka, T. Doi, T. Abe, Z. Ogumi, *J. Phys. Chem. C* **2011**, *115*, 25484–25489
- [33] G. Zampardi, F. La Mantia, W. Schuhmann, *RSC Adv.* **2015**, *5*, 31166–31171
- [34] P. Lu, C. Li, E. W. Schneider, S. J. Harris, *J. Phys. Chem. C* **2014**, *118*, 896–903
- [35] O. Matsuoka, A. Hiwara, T. Omi, M. Toriida, T. Hayashi, C. Tanaka, Y. Saito, T. Ishida, H. Tan, S. S. Ono, S. Yamamoto, *J. Power Sources* **2002**, *108*, 128–138
- [36] M. Tang, J. Newman, *J. Electrochem. Soc.* **2011**, *158*, A530–A536
- [37] M. Tang, J. Newman, *J. Electrochem. Soc.* **2012**, *159*, A281–A289
- [38] R. R. Jaini, B. P. Setzler, A. G. Star, T. F. Fuller, *J. Electrochem. Soc.* **2016**, *163*, A2185–A2196
- [39] M. T. Dinh-Nguyen, C. Delacourt, *J. Electrochem. Soc.* **2016**, *163*, A706–A713
- [40] D. Strmcnik, I. E. Castelli, J. G. Connell, D. Haering, M. Zorko, P. Martins, P. P. Lopes, B. Genorio, T. Østergaard, H. A. Gasteiger, F. Maglia, B. K. Antonopoulos, V. R. Stamenkovic, J. Rossmeisl, N. M. Markovic, *Nat. Catal.* **2018**, *1*, 255–262
- [41] H. E. Hoster, *Nat. Catal.* **2018**, *1*, 236–237
- [42] C. Ashworth, *Nat. Rev. Mater.* **2018**, *3*
- [43] D. Lu, M. Xu, L. Zhou, A. Garsuch, B. L. Lucht, *J. Electrochem. Soc.* **2013**, *160*, A3138–A3143
- [44] M. Xu, L. Zhou, Y. Dong, Y. Chen, A. Garsuch, B. L. Lucht, *J. Electrochem. Soc.* **2013**, *160*, A2005–A2013
- [45] Y.-C. Lu, A. N. Mansour, N. Yabuuchi, Y. Shao-Horn, *Chem. Mater.* **2009**, *21*, 4408–4424
- [46] Y. Park, S. H. Shin, H. Hwang, S. M. Lee, S. P. Kim, H. C. Choi, Y. M. Jung, *J. Mol. Struct.* **2014**, *1069*, 157–163
- [47] M.-J. Kim, J.-T. Yeon, K. Hong, S.-I. Lee, N.-S. Choi, S.-S. Kim, *Bull. Korean Chem. Soc.* **2013**, *34*, 2029–2035
- [48] H. Bryngelsson, M. Stjernholm, T. Gustafsson, K. Edström, *J. Power Sources* **2007**, *174*, 970–975
- [49] R. Dedryvere, H. Martinez, S. Leroy, D. Lemordant, F. Bonhomme, P. Biensan, D. Gonbeau, *J. Power Sources* **2007**, *174*, 462–468
- [50] V. Eshkenazi, E. Peled, L. Burstein, D. Golodnitsky, *Solid State Ionics* **2004**, *170*, 83–91
- [51] M. Xu, D. Lu, A. Garsuch, B. L. Lucht, *J. Electrochem. Soc.* **2012**, *159*, A2130–A2134
- [52] M. Nie, B. L. Lucht, *J. Electrochem. Soc.* **2014**, *161*, A1001–A1006
- [53] L. Yang, B. Ravdel, B. L. Lucht, *Electrochim. Solid-State Lett.* **2010**, *13*, A95–A97
- [54] M. Herstedt, D. P. Abraham, J. B. Kerr, K. Edström, *Electrochim. Acta* **2004**, *49*, 5097–5110
- [55] K. Edström, M. Herstedt, D. P. Abraham, *J. Power Sources* **2006**, *153*, 380–384
- [56] A. M. Andersson, A. Henningson, H. Siegbahn, U. Jansson, K. Edström, *J. Power Sources* **2003**, *119*, 522–527
- [57] A. v. Cresce, S. M. Russell, D. R. Baker, K. J. Gaskell, K. Xu, *Nano Lett.* **2014**, *14*, 14045–1412
- [58] H. Ota, K. Shima, M. Ue, J.-i. Yamaki, *Electrochim. Acta* **2004**, *49*, 565–572
- [59] K. Xu, *Chem. Rev.* **2004**, *104*, 4303–4418
- [60] D. Aurbach, B. Markovsky, I. Weissman, E. Levi, Y. Ein-Eli, *Electrochim. Acta* **1999**, *45*, 67–86
- [61] K. Tasaki, A. Goldberg, J.-J. Lian, M. Walker, A. Timmons, S. J. Harris, *J. Electrochem. Soc.* **2009**, *156*, A1019–A1027
- [62] D. Aurbach, M. D. Levi, E. Levi, A. Schechter, *J. Phys. Chem. B* **1997**, *101*, 2195–2206
- [63] N. G. Tsierkezos, *J. Solution Chem.* **2007**, *36*, 289–302
- [64] G. Zampardi, E. Ventosa, F. La Mantia, W. Schuhmann, *Chem. Commun.* **2013**, *49*, 9347–9349
- [65] K. M. Abraham, D. M. Pasquariello, E. B. Willstaedt, *J. Electrochem. Soc.* **1990**, *137*, 1856–1857
- [66] N. Tsierkezos, U. Ritter, *J. Appl. Electrochem.* **2010**, *40*, 409–417
- [67] C. Cannes, F. Kanoufi, A. J. Bard, *J. Electroanal. Chem.* **2003**, *547*, 83–91
- [68] M. Nádherná, J. Reiter, *Electrochim. Acta* **2010**, *55*, 5911–5916
- [69] H. Matsuda, Y. Ayabe, *Zeitschrift für Elektrochemie, Ber. Bunsenges. Phys. Chem.* **1955**, *59*, 494–503
- [70] A. J. Bard, L. R. Faulkner, *Electrochemical methods. Fundamentals and applications*, 2nd ed., Wiley, New York, 2001.
- [71] C. H. Hamann, A. Hammett, W. Vielstich, *Electrochemistry*, 2nd ed., Wiley-VCH Verlag GmbH & Co. KGaA, 2007.
- [72] C. O. Laoire, E. Plichta, M. Hendrickson, S. Mukerjee, K. M. Abraham, *Electrochim. Acta* **2009**, *54*, 6560–6564
- [73] J. P. Schmidt, P. Berg, M. Schönleber, A. Weber, E. Ivers-Tiffée, *J. Power Sources* **2013**, *221*, 70–77
- [74] J. P. Schmidt, T. Chrobak, M. Ender, J. Illig, D. Klotz, E. Ivers-Tiffée, *J. Power Sources* **2011**, *196*, 5342–5348

- [75] D. Moosbauer, S. Zugmann, M. Amereller, H. J. Gores, *J. Chem. Eng. Data* **2010**, *55*, 1794–1798
- [76] M. D. Levi, G. Salitra, B. Markovsky, H. Teller, D. Aurbach, U. Heider, L. Heider, *J. Electrochem. Soc.* **1999**, *146*, 1279–1289
- [77] D. Aurbach, M. D. Levi, E. Levi, H. Teller, B. Markovsky, G. Salitra, U. Heider, L. Heider, *J. Electrochem. Soc.* **1998**, *145*, 3024–3034
- [78] Y. Yamada, K. Miyazaki, T. Abe, *Langmuir* **2010**, *26*, 14990–14994
- [79] M. Winter, J. O. Besenhard, M. E. Spahr, P. Novák, *Adv. Mater.* **1998**, *10*, 725–763
- [80] P. Niehoff, S. Passerini, M. Winter, *Langmuir* **2013**, *29*, 5806–5816
- [81] G. Zampardi, F. La Mantia, W. Schuhmann, *Electrochim. Commun.* **2015**, *58*, 1–5
- [82] A. Wang, S. Kadam, H. Li, S. Shi, Y. Qi, *npj Comput. Mater.* **2018**, *4*, 15–40
- [83] S. Shi, P. Lu, Z. Liu, Y. Qi, L. G. Hector, H. Li, S. J. Harris, *J. Am. Chem. Soc.* **2012**, *134*, 15476–15487
- [84] A. Zaban, D. Aurbach, *J. Power Sources* **1995**, *54*, 289–295
- [85] E. Peled, D. Golodnitsky, G. Ardel, *J. Electrochem. Soc.* **1997**, *144*, L208–L210
- [86] D. Li, D. Danilov, Z. Zhang, H. Chen, Y. Yang, Notten, P. H. L., *J. Electrochem. Soc.* **2015**, *162*, A858–A869
- [87] A. P. Abbott, C. L. Miaw, J. F. Rusling, *J. Electroanal. Chem.* **1992**, *327*, 31–46
- [88] A. D. Clegg, N. V. Rees, O. V. Klymenko, B. A. Coles, R. G. Compton, *J. Electroanal. Chem.* **2005**, *580*, 78–86
- [89] B. Sakintuna, O. Çuhadar, Y. Yürüm, *Energy Fuels* **2006**, *20*, 1269–1274
- [90] B. K. Antonopoulos, A.-C. Gentschev, F. Maglia, H. E. Hoster, *Manuscript in preparation*.
- [91] H. J. Ploehn, P. Ramadass, R. E. White, *J. Electrochem. Soc.* **2004**, *151*, A456–A462
- [92] B. K. Antonopoulos, C. Stock, F. Maglia, H. E. Hoster, *Electrochim. Acta* **2018**, *269*, 331–339

Manuscript received: May 7, 2018

Accepted Article published: June 20, 2018

Version of record online: July 22, 2018